Design and Simulation of Microptical Devices (Spot Displacement Devices) for Free-Space All-Optical OXC Systems

Victor Argueta-Diaz, *Member, IEEE*, and Betty Lise Anderson, *Senior Member, IEEE*

***Abstract*—We introduce two new designs for a spot displacement device (SDD) to be used in a White cell-based binary optical cross-connect system (OXC). We described in detail the implementation of an SDD based on a lens train configuration and a roof prism SDD. We discuss the aberrations associated with each design. We also show simulations for an eight-output OXC binary system using one of these designs.**

***Index Terms*—Lens waveguides, optical communications, optical switches.**

I. Introduction

OPTICAL cross-connects (OXCs) have become a critical network element for constructing the next generation of optical network, where provisioning (reconfiguration), scalability, and fast restoration will be needed [1]–[3]. The main attraction of all-optical switching is that it enables routing of optical data signals without the need for conversion to electrical signals, and therefore, is independent of data rate and data protocols [4], [5].

Several solutions are currently under research. We are particularly interested in those solutions involving microelectromechanical systems (MEMS) technology, although we acknowledge other possibilities [6]–[9]. MEMS, however, are an attractive technology that allows optical switching for a large number of ports with low loss and low cost per port [10]. In general, MEMS OXC solutions can be divided into two main groups: two-dimensional (2-D) digital MEMS and three-dimensional (3-D) analog MEMS. In 2-D digital MEMS, the switches are integrated in a 2-D array of micromirrors on a silicon substrate where the beams are propagating parallel to the substrate. Depending on the MEMS, the micromirrors can be tilted, rotated, or lifted into and out of the optical path to change the propagation direction of the optical beam from a particular input [11], [12].

OXCs using 3-D analog MEMS allow for a higher number of ports. In the literature, we can find several examples where these systems have been implemented successfully [13]–[18]. We can say, however, that these systems require a very precise control for the micromirrors. In some cases an accuracy of tens of microradians is necessary [16], [17], [19]. The required control system will increase in complexity as the number of ports increases. To the best of the authors' knowledge, no systems have been implemented using a digital MEMS in 3-D architectures. This proposed combination may have the advantage of simplifying the control system while conserving a higher number of ports.

We have proposed previously in [20] and [21] a new approach to the OXC problem. Our architecture is a free-space 3-D while still using digital MEMS. Our system is based on the optical White cell [22], [23], which consists of three spherical mirrors among which light can circulate. On each pass, the beams inside the White cell are refocused on one of the mirrors in a unique spot pattern. We substitute this mirror with an MEMS, so that the focused beams can land on individual micromirrors, giving us the flexibility to switch a beam to a new destination on each pass.

The system presented in this paper switches the beam to a new output by means of a device that we call "spot displacement device" (SDD). Here, we present new designs for an SDD where we have reduced the aberrations. Each design is evaluated in terms of aberrations where the SDDs are configured to provide displacements of 500 and 2000 μm. From this evaluation, we will use the design with the lowest abberations and simulate an 1×8 OXC system. The evaluation of the SDD will also help us to estimate the scalability of our system with the proposed design.

In Section II, we will briefly mention the basic characteristics of the binary White cell OXC configuration. In Section III, we will discuss a previously proposed design and introduce two new designs for the SDD. We will analyze the propagation of a Gaussian beam through the new designs and detect limits in propagations and tolerances for different misalignments. In Section IV, we will present the simulations of each of our designs for two different displacements (i.e., 500 and 2000 μm). These simulations will help us to evaluate the aberration performance of each of the designs. The design with the best performance is then simulated in a binary OXC system in Section V. We will simulate an eight-ouput binary OXC system and present the results in terms of aberrations for each one of the outputs. Finally, in Section VI, we will present the summary and conclusions of our work.

II. Binary White Cell OXC

Our proposal is a new architecture in which we can create spot shifts using a White cell with a two-state (or three-state

Manuscript received March 7, 2005; revised March 20, 2006 and April 6, 2006.

The authors are with the Department of Electrical and Computer Engineering, The Ohio State University, Columbus, OH 43210 USA (e-mail: argueta-diaz.1@osu.edu).

Digital Object Identifier 10.1109/JSTQE.2006.876162

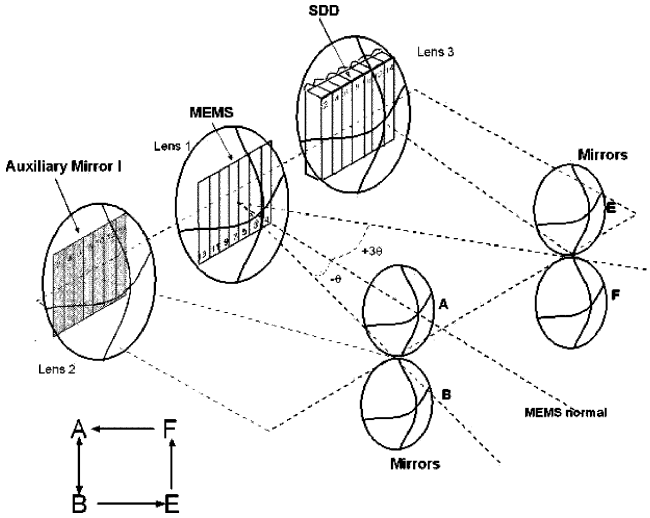

Fig. 1. Binary White cell OXC configuration.

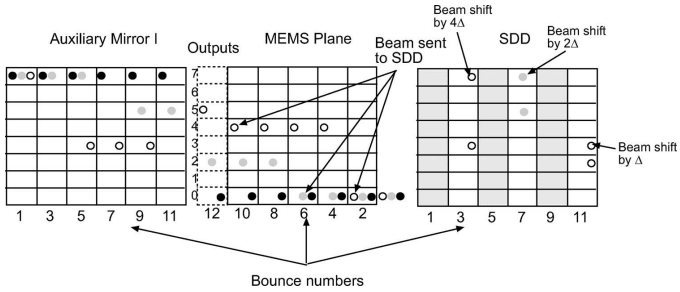

Fig. 2. Spot pattern for multiple inputs in the binary White-cell-based OXC.

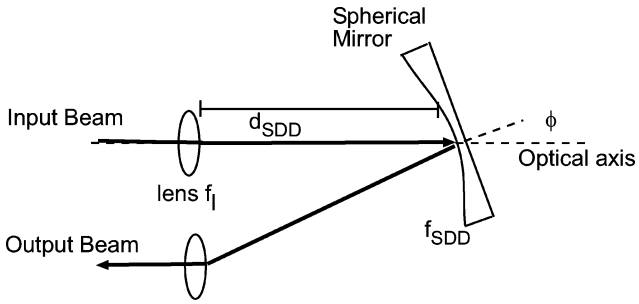

Fig. 3. Lens spherical mirror combination.

MEMS), using what we called an SDD. In this section, we will briefly mention the binary White cell and the role of the SDD, but in the interest of providing a wider background, we refer the reader to [20], [21], and [24].

Previously, we have reported the OXC system, shown in Fig. 1, based on the White cell. Our goal is to perform optical switching, which we will do by allowing several input beams to be switched between two different White cells. One White cell maintains the beams spots in their current row (null displacement), whereas the second White cell redirects the beam to a new row (output). The null cell is formed in Fig. 1 by the mirrors A and B, the MEMS, and auxiliary mirror I. The second White cell, formed by the mirrors E and F, the MEMS, and the SDD, will change each beam to a different row. The switching between the White cell is done via the MEMS.

The SDD shifts the beams down to a specific distance. The shifting of spots will eventually result in beams leaving the device at different locations. The number of pixels by which a beams is shifted will be different for each SDD column. That is, each SDD will shift the beam by a distance equal to twice that of the shift produced by the previous column. One column will produce a shift of Δ, the next column a shift of 2Δ, the next after a shift of 4Δ, and so on, thus producing a binary system.

By shifting the spots, we can control the row at which any given beam reaches the output turning mirror, and we associate each row with a different output. The number of possible outputs is determined by the total number of possible shifts for a given number of bounces. In the design of Fig. 1, a shift is made every time the beam goes to the SDD, but this can only happen once every four bounces. Thus, the number of outputs N is given by $N_{\text{binary}} = 2^{m/4}$, where m is the number of bounces.

It is important to mention that we will refer as "shift" to any change in position in the SDD and MEMS plane. This shift will be a multiple of the micromirrors pitch Δ. Therefore, the SDD will cause a shift of $\Delta, 2\Delta, 4\Delta$, etc. We make this distinction to clarify the shift caused by the SDD and the MEMS pitch.

For a better understanding of how the SDD causes the shift of a beam in the binary White cell, we reproduce an example shown previously in [21]. For sake of argument, let us assume that we need to send the "white" beam to the fifth output. Therefore, we will need to send the "white" beam to the SDD two times to cause a shift of 4Δ and Δ on the beam position. The "white" beam starts bouncing in the AB White cell (null cell) until the second one when the beam is sent to the SDD. Then the "white" beam goes through the SDD, which for that particular column has a value of 4Δ. After this SDD, the beam is sent back to the MEMS on the fourth row instead of the zeroth row. We then keep bouncing the "white" beam in the AB White cell, until the tenth bounce, when we again send the beam to the SDD. This time, however, the SDD causes a shift of Δ, and so, after this second SDD, the beam is shifted an additional row. Therefore, the beam is now at the fifth row (output) where it remains by keeping bouncing in the null cell. In a similar way, we can send the "gray" beam to the second output and the "black" beam to the zeroth output (Fig. 2).

III. SDD Designs

In this paper, we describe new ways to produce the spot displacement to improve the SDDs that were developed before. We also discussed in this paper how the shifts were produced and what imaging conditions were required to achieve the necessary pitch displacement (Δ) on the MEMS plane.

To provide enough clarification to the reader, we will include some of the original work developed in [21] and expand on the analysis of the tilted spherical mirror SDD, shown in Fig. 3. Later, we will introduce two new designs. We will analyze these three designs in terms of misalignment tolerances and aberrations.

The first step to create the binary cross-connection device is to design an SDD. The basic function of the SDD is to cause a displacement in an incident beam. The SDD shifts the spot onto a new row on the MEMS plane. Depending on which bounce the beam is sent to the SDD, the beam will have a different displacement.

We have two main criteria for our SDD designs.

- Each column of the SDD must produce double the displacement of the previous one (1 for the first one).
- Beams in a specific column on the SDD cannot overlap with any adjacent column.

Imaging conditions also need to be fulfilled. The study developed in [21] shows that we can design the SDD independently from the White cell. The SDD can change the position of the beam and still meet the imaging conditions of the White cell, as long as the beams at the input and output planes of the SDD have the same spot size and angle of propagation.

A. Spherical Mirror SDD

A simple approach to create the spot shift is described in detailed in [21] and summarized in the present section. This SDD called tilted spherical mirror SDD is shown in Fig. 3 and is based on the combination of a lens and a spherical mirror.

In the figure, d_{SDD} is the distance between the lens and the tilted spherical mirror, ϕ is the tilted angle of the spherical mirror, f_{SDD} is the focal length of the spherical mirror, and f_l is the focal length of the lens. We will place the lens in the plane of auxiliary mirror II. The light travels through lens f_1, translates a distance d_{SDD}, is reflected by the spherical mirror of focal length f_{SDD}, which is tilted ϕ radians, and goes back toward the spherical mirror E in Fig. 1.

This system can be described using paraxial Gaussian beam equations. The relationship of the beam parameters before (q_0) and after SDD (q_1) is given by

$$q_1 = \frac{Aq_0 + B}{Cq_0 + D} \tag{1}$$

where A, B, C, and D are the elements of the ray transfer matrix of the system under study. The optical system consists of the microlens, the spherical mirror, and the translation between these two elements. From [21], we know that this system generates a focus image of the input beam, that is $q_1 = q_0$ when $f_l = d_{\text{SDD}}$ and $f_{\text{SDD}} = d_{\text{SDD}}/2$. The question now is, "How tolerant is the system to misalignments on the output plane?"

To estimate this tolerance, we will presuppose that the output is displaced a distance δ from its ideal value. This additional distance produces two effects. First, the beam size will increase due to the diffraction of the Gaussian beam, and second, the q_1 parameter at the output beam will not be purely imaginary.

We measure how the change in distance δ affects the output Gaussian beam by comparing it against the input Gaussian beam. This change can be measured by the overlap integral η of the two beams. If the input and output beams are equal, then $\eta = 1$. The overlap integral between the input Gaussian wave function $\phi(x, y)$ and the output Gaussian function $\psi(x, y)$ is given by

$$\eta = \frac{\left|\int_{-\infty}^{\infty}\int \phi(x,y)\psi^*(x,y)\,dx\,dy\right|^2}{\int_{-\infty}^{\infty}\int \phi(x,y)\phi^*(x,y)\,dx\,dy \int_{-\infty}^{\infty}\int \psi(x,y)\psi^*(x,y)\,dx\,dy} \tag{2}$$

where

$$\phi(x,y) = \exp\left[-\frac{x^2+y^2}{w_0^2}\right]$$
$$\psi(x,y) = \exp\left[-\frac{x^2+y^2}{w_1^2}\right]\exp\left[-ik\frac{x^2+y^2}{2R_1}\right] \tag{3}$$

where $\phi(x, y)$ and $\psi(x, y)$ are complex Gaussian beams with normalized amplitude. We assume that the wavefront of $\phi(x, y)$ has an infinite radius of curvature, and that the wavefront of $\psi(x, y)$ has a finite radius of curvature R_1.

Solving (1) for the tilted spherical mirror SDD with a δ lateral displacement give us

$$q_1 = q_0 + \delta \tag{4}$$

and solving for R and w_1, we get

$$w_1^2 = \frac{\lambda^2\delta^2 + \pi^2 w_0^4}{\pi^2 w_0^2} \tag{5}$$

$$R = \frac{\lambda^2\delta^2 + \pi^2 w_0^4}{\lambda^2\delta}. \tag{6}$$

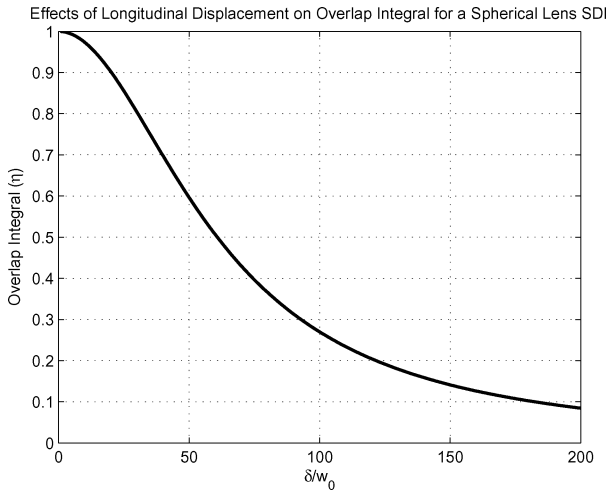

Fig. 4. Coupling efficiency for a spherical mirror SDD versus longitudinal displacement.

Fig. 4 shows the overlap integral for different values of δ normalized to the spot size w_0. It is seen that we have a 20% loss in the overlap integral when the longitudinal displacement δ has a value 30 times the spot size (for a 15-μm spot size, this value corresponds to a δ displacement of 450 μm). We are assuming $\lambda = 1.55$ μm. Thus, we can conclude that the losses are very forgiving of misalignments.

Furthermore, because the shift is caused only by the tilting angle of the spherical mirror, the $ABCD$ matrix of the system remains the same regardless of the tilting angle. Therefore, the coupling efficiency graph shown in Fig. 4 is independent of

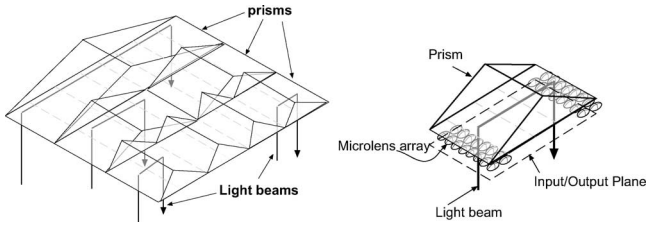

Fig. 5. Roof prism SDD on the input/output plane of the SDD.

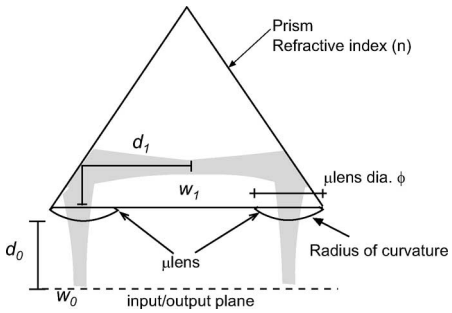

Fig. 6. Input/output plane on roof prism SDD.

the required shift Δ. This particular SDD has a very simple geometry and its design is somewhat similar to that of the White cell, in the sense that is takes free-space beams and refocuses them in the desired position by tilting a spherical mirror, which makes this SDD an appealing option to choose. We will see, however, in Section IV than the implementation of this SDD is more problematic than it seems.

B. Roof Prism SDD

A new design for an SDD is shown in Fig. 5. In this approach, a series of microprisms are substituted for the SDDs in the binary White cell OXC. In front of these microprisms, an array of microlenses are used to reduce the divergence of the beams coming from the White cell. As the beams travel through the microprism, they are redirected to a new position where another set of microlenses are used to send the beams again to the White cell with the same characteristics (i.e., spot size, divergence) as they came in with.

The microlenses prevent the beams from overlapping to adjacent prisms while travelling through their corresponding SDD column by reducing the divergence of the beams. We can see in Fig. 6 that the light coming from the White cell is focused at the SDD input/output plane. The microlenses are placed at a distance d_0 after this plane. As the input and output microlenses are symmetrical, we expect to have the beam waist of the collimated beam w_1' at the middle point. This middle point is located at an optical path distance d_1 from the microlens. The input beam has a spot size w_0. Each microlens has a diameter Φ and a radius of curvature $R_{\rm ml}$. The microprism has a refractive index n, which we will assume to be equal to that of the microlenses.

From Fig. 6, we can reduce our problem of finding the microlens that transforms a Gaussian beam with beam waist radius w_0 at a distance d_0 in front of the lens to another with a waist w_1' at d_1 and back to the original beam (with a spot size w_1) through a symmetrical optical path. The optical system consists of the microlens, a translation through the prism space, and the second microlens. We solve (1) by separating the real and imaginary elements

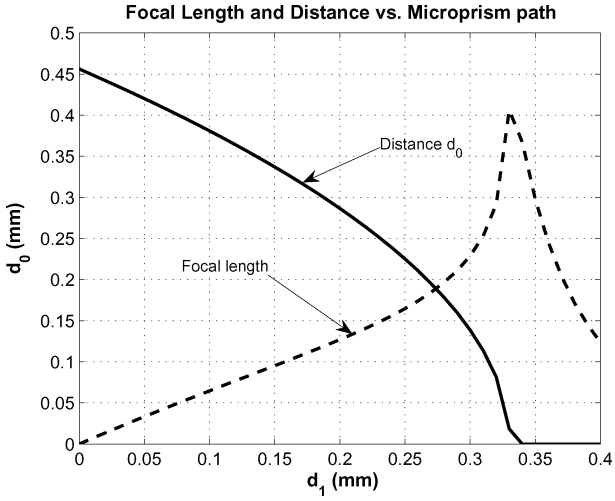

Fig. 7. Focal length and distance d_0 versus distance d_1; dashed line: radius of curvature; solid line: distance d_0. $w_0 = 15$ μm, $\lambda = 1.55$ μm, and $n = 1.449624$.

$$
\begin{aligned}
0 = {} & \frac{2d_0 - 2d_0^2 n}{R_{\rm ml}} + \frac{2d_0^2}{R_{\rm ml}} + \frac{4d_1 d_0}{nR_{\rm ml}} - \frac{4d_1 d_0}{R_{\rm ml}} - \frac{4d_1 d_0^2}{R_{\rm ml}^2} \\
& + \frac{2d_1 d_0^2 n}{R_{\rm ml}^2} + \frac{2d_1 d_0^2}{R_{\rm ml}^2 n} + \frac{2d_1}{n} - \frac{2q_0 q_1 n}{R_{\rm ml}} + \frac{2q_0 q_1}{R_{\rm ml}} \\
& - \frac{4q_0 q_1 d_1}{R_{\rm ml}^2} + \frac{2q_0 q_1 d_1 n}{R_{\rm ml}^2} + \frac{2q_0 q_1 d_1}{R_{\rm ml}^2 n} \qquad (7) \\
0 = {} & q_0 - q_1 - \frac{2q_0 d_0 n}{R_{\rm ml}} + \frac{2q_0 d_0}{R_{\rm ml}} + \frac{2q_0 d_1}{R_{\rm ml} n} - \frac{2q_0 d_1}{R_{\rm ml}} \\
& - \frac{4q_0 d_1 d_0}{R_{\rm ml}^2} + \frac{2q_0 d_1 d_0 n}{R_{\rm ml}^2} + \frac{2q_0 d_1 d_0}{R_{\rm ml}^2 n} + \frac{2q_1 d_0 n}{R_{\rm ml}} \\
& - \frac{2q_1 d_0}{R_{\rm ml}} - \frac{2q_1 d_1}{R_{\rm ml} n} + \frac{2q_1 d_1}{R_{\rm ml}} + \frac{4q_1 d_1 d_0}{R_{\rm ml}^2} \\
& - \frac{2q_1 d_1 d_0 n}{R_{\rm ml}^2} - \frac{2q_1 d_1 d_0}{(R_{\rm ml}^2 n)}. \qquad (8)
\end{aligned}
$$

At the beam waist, not only are the complex parameters q_0 and q_1 purely imaginary (i.e., the wavefront's radius of curvature is ∞), but for 1:1 magnification, we also require $q_1 = q_0$. Therefore, the Gaussian transformation can be described by solving (7) and (8) for $R_{\rm ml}$ and d_0, shown in (9) and (10) at the bottom of the next page.

Fig. 7 shows the possible values of d_0 and the focal length of the microlens (defined as $f = R_{\rm ml}/(n-1)$) as a function of d_1. We propose that the microprism and microlenses are made of polymethylmethacrylate (PMMA), which has a refractive index of $n = 1.449624$ at the rate of 1.55 μm. We chose PMMA because it is a polymer that has been tested successfully in the fabrication of interconnection structures, as a substrate for polymer

optoelectronic devices and integrated waveguides [25]–[27]. We also assume that the light source has a spot size $w_0 = 15\ \mu$m and a wavelength $\lambda = 1.550\ \mu$m. In the graph, we can also see the point of intersection between distance d_0 and the focal length f, which represents a $4f$ imaging system. The value of d_1 is set at 0.2738 mm, and that of d_0 at 0.1889 mm for this specific case.

We will like to work with a $4f$ imaging system because of the symmetry that the system presents. Solving (7) and (8) to find the intersection point for a general system (i.e., the object is located at the focal length of the microlens) we get

$$R = \frac{(n-1)d_1}{n} \tag{11}$$

$$d_0 = \frac{d_1}{n}. \tag{12}$$

There is a limit, however, in the extension of this imaging system. The limit is imposed by the diameter of the microlens. To have a clear aperture, we would like the microlens radius $\Phi/2$ to be at least $2w(z)$ to capture 99.9% of the incoming light, where $w(z)$ is the spot size radius of the beam at the microlens position. Assuming the Gaussian beam propagation described in [28], the limit in d_0 is set as

$$d_0 < \frac{\pi w_0^2}{\lambda}\sqrt{\left(\frac{\Phi}{4w_0}\right)^2 - 1}. \tag{13}$$

Another question to answer is what is the effect of any change in the distance d_1 from its ideal value. We will now investigate the consequences of a change of the distance between the two lenses in a $4f$ imaging system. As in the spherical mirror SDD case, the additional distance between the two curved surfaces in the microprism will produce a larger beam with a finite radius of curvature.

Let us consider a distance $2d_1 = 2f + \delta$ between the two lenses. We will also require $w_1 = w_0$. Using ray matrices and replacing $2d_1$ by $2f + \delta$, the $ABCD$ matrix for the $4f$ system gives

$$R_1 = -\frac{f^2}{2n\delta}. \tag{14}$$

Equation (2) becomes

$$\eta = \frac{\left|\int_{-\infty}^{\infty}\int \exp\left(\left[-\frac{2}{w^2} - i\frac{k}{2R_1}\right](x^2+y^2)\right)dx\,dy\right|^2}{\left|\int_{-\infty}^{\infty}\int \exp\left[-\frac{2}{w^2}(x^2+y^2)\right]dx\,dy\right|^2} = \frac{1}{1+(k^2w^4/16R_1^2)}. \tag{15}$$

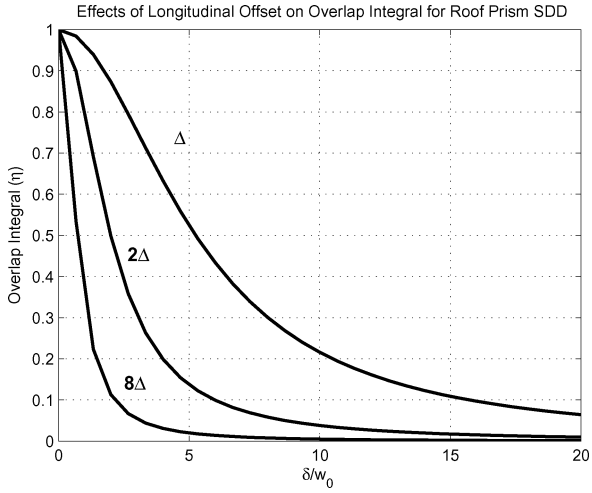

Fig. 8. Coupling efficiency for a roof prism SDD versus longitudinal displacement for different shifts (Δ).

Substituting (14) into (15) and using $z_r = \pi w_0^2/\lambda$, we obtain

$$\eta = \frac{1}{1+(n\delta z_r/f^2)^2}. \tag{16}$$

Fig. 8 shows the overlap integral for the longitudinal displacement δ for three different shifts ($\Delta, 2\Delta$, and 8Δ). The graph is normalized to the spot size w_0. For the particular values of δ shown in the figure, the points where we get a 20% loss in the overlap integral are $\delta/w_0 = 2.6235, \delta/w_0 = 0.9847$, and $\delta/w_0 = 0.2872$ (which correspond to values of $\delta_1 = 0.03935$ mm, $\delta_2 = 0.01477$ mm, and $\delta_3 = 0.00431$ mm for $w_0 = 15\ \mu$m) for $\Delta, 2\Delta$, and 8Δ, respectively. We are assuming $n = 1.449624$, $z_r = 0.4560$ mm, and $\lambda = 1.55\ \mu$m, which corresponds to a Gaussian beam with the characteristics mentioned for Fig. 7. Thus, the misalignment losses increases with the required shift. It is important to note that any error in the distance d_1 will cause a change in the radius of curvature of the wavefront, and not in the spot size. To have a proper imaging system, however, it would be necessary to have the correct radius of curvature at the imaging planes.

Tighter tolerances are found when we analyze the transverse offset, however. This offset occurs when the input beam in not completely on the optical axis. For this case, the input Gaussian beam is described by

$$\phi(x,y) = \exp\left[-\frac{(x+\epsilon)^2+y^2}{w_0^2}\right]. \tag{17}$$

The overlap integral using (2) shows how the coupling efficiency decreases with increasing transverse offset ϵ between the two Gaussian beams (we are assuming that there is no

$$R_{\mathrm{ml}} = \frac{q_0^2 n + d_0^2 n + 2d_1 d_0 - \sqrt{q_0^4 n^2 + 2q_0^2 d_0^2 n^2 + d_0^4 n^2 - 4q_0^2 d_1^2 (n-1)}}{2(d_1 + d_0 n)} \tag{9}$$

$$d_0 = \left[\frac{q_0 q_1 n - 2d_1\sqrt{q_0 q_1}}{n}\right]^{1/2} \tag{10}$$

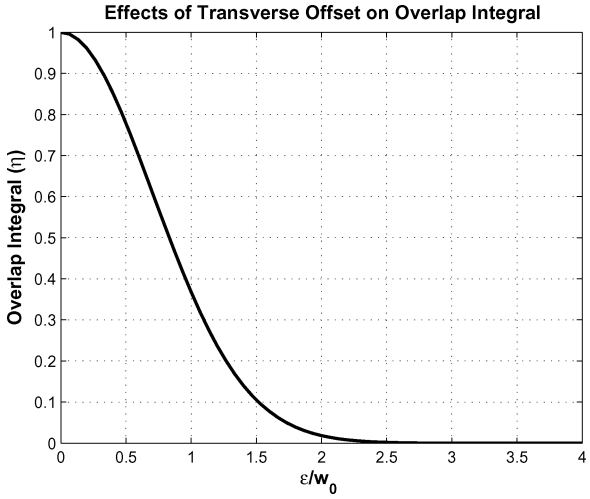

Fig. 9. Coupling efficiency for a roof prism SDD versus transverse displacement.

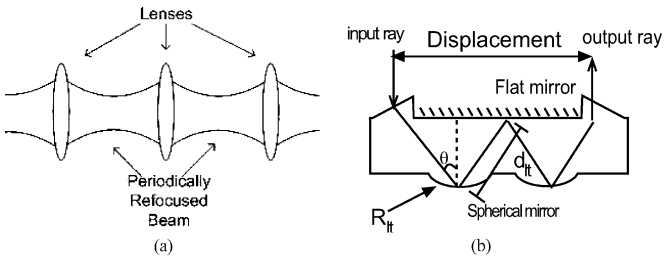

Fig. 10. Lens train SDD.

longitudinal displacement, and so the graph is independent of the shift). A 20% overlap integral loss is caused for an offset of only 0.4724 w_0, which corresponds to only 7.086 μm for $w_0 = 15$ μm. The effects of the transverse offset can be seen in Fig. 9. This tolerance is important because it will indicate how far off the SDD can be from the optical axis.

C. Lens Trains SDD

The last design that we will discuss is based on a modified optical waveguide built with lenses, Fig. 10(a). In the figure, we show a set of identical lenses of focal length f separated by a distance d. From [29], we know that this system is stable when the distance between lenses does not exceed four times the focal length of the lenses.

We want to take advantage of this stability; so, we can propagate a beam through long distances and, therefore, have longer displacements on the MEMS plane. In Fig. 10(b), we show how we divide the lens waveguide in two planes. In the upper plane, we have placed a flat mirror, while in the lower plane is a series of spherical mirrors. Light will bounce between the spherical mirrors the same way it travelled through the lenses. The optical path $d_{\rm lt}$ in Fig. 10(b) between the spherical mirrors and the flat mirror has to be less than $R_{\rm lt}$, where $R_{\rm lt}$ is the radius of curvature of the spherical mirror that is defined as $f_{\rm lt} = R_{\rm lt}/2$ to fulfill the stability condition.

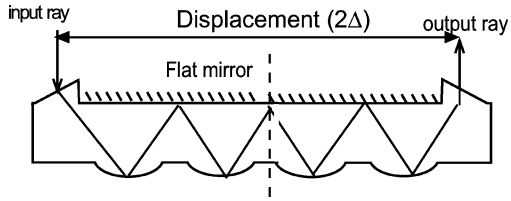

Fig. 11. 2Δ pitch lens train SDD.

We can also see from Fig. 10(b) that the input/ouput plane has a prism-shaped entrance/exit. The prism-shaped entrance deflects the incoming light to the first spherical mirror on the device, while the prism-shaped exit returns the beam to the White cell with the equal and opposite angle as it went in with (to mimic a physical mirror). This causes the light to be displaced in an orthogonal plane while being confined by the spherical mirrors. This propagation will represent, eventually, the desired displacement on the MEMS plane.

The distance $d_{\rm lt}$ will be limited by the divergence of the beam. To calculate the maximum distance $d_{\rm lt}$, we have to consider the spot size at the spherical mirrors on the SDD. The distance $d_{\rm lt}$ in Fig. 10(b) will be the distance in which the size of the beam at the input plane on the spherical mirror SDD doubles. This distance was established already in [21] and the shift after each reflection inside the SDD can then be calculated as

$$\Delta' = 2\sqrt{3}\frac{\pi w_0^2}{\lambda}\sin\theta \tag{18}$$

where θ is the angle of the input beam with respect to the normal of the spherical mirror as shown in Fig. 10(b).

In case we need a bigger shift, instead of modifying θ or $d_{\rm lt}$ as in the design described in Section III-B, it is only necessary to repeat this structure (that we call "unit cell") as many times as needed until the required shift is reached. Fig. 11 shows an SDD lens train device for a 2Δ displacement, which is build up by two equal structures. Similar to the SDD of Section III-B, we can define each structure as a $4f$ imaging system; the problem is then reduced to analyzing consecutive $4f$ imaging systems.

We will use again the overlap integral to measure the effect of the offset δ and compare the results of this section to the ones obtained in Section III-B. Substituting $d_{\rm lt} = 2(f+\delta)$ in the ABCD matrix for this $4f$ system and substituting this result into (1), we obtain

$$q_1 = \frac{-nq_0 f_{\rm lt}^2 + nq_0\delta^2 - 2f_{\rm lt}^2\delta + \delta^3}{n(n\delta q_0 + \delta^2 - f_{\rm lt}^2)}. \tag{19}$$

Solving for R_1 and w_1^2, which are the radius of curvature of the Gaussian beam and the spot size defined in [28], and using (19)

$$R_1 = \frac{q_0^2 n^2 (f^2-2\delta^2)^2 - 4\delta^2(f^2-\delta^2)^2}{-2n^3\delta(f^2-2\delta^2)q_0^2 - 2n\delta(f^2-\delta^2)} \tag{20}$$

$$w_1^2 = \frac{\left[q_0^2 n^2 (f^2-2\delta^2)^2 - 4\delta^2(f^2-\delta^2)^2\right]\lambda^2}{n^2 f^4 \pi^2 w_0^2}. \tag{21}$$

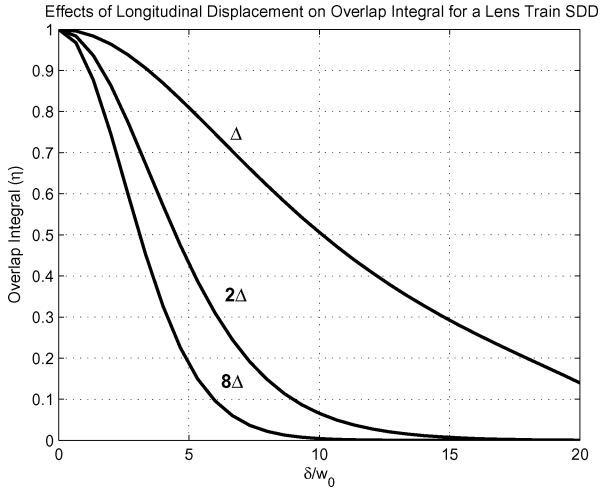

Fig. 12. Overlap integral for different shifts (Δ) versus longitudinal offset.

Substituting (20) and (21), the overlap integral described in (2) becomes

$$\eta = \frac{4w_0^2 w_1^2}{\left(w_0^2 + w_1^2\right)^2 + (k w_1^2 w_0^2/2R)^2} \tag{22}$$

where $k = 2\pi/\lambda$.

Fig. 12 shows the effect for a longitudinal displacement in the coupling efficiency for three different shifts ($\Delta, 2\Delta$, and 8Δ). The overlap integral varies depending on the required shift. For the particular values of Δ shown in the figure, the points where we get a 20% loss in the overlap integral are $\delta/w_0 = 5.1534, \delta/w_0 = 2.4705$, and $\delta/w_o = 1.7255$ (which correspond to a value of $\delta_1 = 0.0773$ mm, $\delta_2 = 0.03706$ mm, and $\delta_3 = 0.02588$ mm for $w_0 = 15$ μm) for $\Delta, 2\Delta$, and 8Δ, respectively. We can appreciate that the tolerances became tighter as we increase the number of unit cells. We can conclude that even though the lens train SDD allows for a simple way to increase the amount of possible shifts, the longitudinal offset tolerances will become more important. It may be possible to have a single unit cell and, instead of repeating the structure, we can modify the angle θ and distance d_{lt}; but in that case, it will be important to study the effects these changes may have on aberrations.

IV. Simulations

In this section, we will evaluate the performance of the different SDD designs discussed in Section III. We will compare the presence of aberrations (mainly astigmatism and spherical aberrations) for two different shifts, 500 and 2000 μm, that represent a shift of 2Δ and 8Δ (assuming a pitch $\Delta = 250$ μm), respectively. This difference in shift distance will help us to evaluate whether there is any dependence of the aberrations on the shift distance, and also it will help to determine which designs are better suited for short and long shift distances.

The following simulations are done in OSLO ray analysis simulation software. The objective is to identify if there is any relation between the amount of displacement caused by the different SDD systems and the aberrations presented.

It is common to represent the effects of aberrations in a graphical representation. There are a number of graphical techniques for representing them. One of the most common representations used is the ray-intercept curve, which represents image-space displacement as a function of object-space fractional coordinates [30], [31]. The shape of the ray-intercept curve indicates not only the amount of aberration but also the specific kind of aberrations that are present in the system. The ordinate for each curve is the height at which the ray-intersects the (paraxial) image plane and the abscissa represent fractions of the aperture plane. Each aberration has a specific ray-trace curve (e.g., coma: parabolid; spherical aberration: cubic curve with a flat near the origin). In case of a perfect-image system, the ray-trace curve is a flat line along the abscissa [32].

Another common graphic representation for astigmatism is the field-trace curve, where a set of principal rays at different object heights are traced. This generates two curves around the paraxial image plane; these curves are the sagittal and tangential image planes. The difference between the tangential and sagittal curves is the astigmatism of the system. If both curves overlap, then no astigmatism is present. The horizontal axis is the distance along the optical axis where the sagittal and tangential images are measured in milimeters and the vertical axis is the fraction of the object plane size [32].

The graphs shown in this section are all divided into three parts. Part 1 is found at the top of each figure. It represents the ray-trace curves for the system. The ray-trace curves are arranged in pairs to show the aberrations for meridional rays (on the left) as well as tangential rays (on the right). Part 2 is found at the middle section of each figure. This graph is the field trace of the system and is used to calculate the astigmatism presented. Two curves representing the tangential and sagittal image positions are shown, where the astigmatism is the distance between these two curves. Finally, part 3 is found at the bottom of each figure. Here, we show a diagram of the system that is being analyzed. For simplicity, we will only label Fig. 13; the remaining figures contain the same parts and only appropriate changes for each system are made.

Based on these results in Section V, we will take the SDD design with the best performance and simulate an eight-output binary White cell OXC. These simulations will help us to evaluate the beam quality at the output plane, and the accumulated aberrations through the system. We assume a wavelength $\lambda = 1.55$ and beam spot size $w_0 = 15$ μm. All SDD designs are assumed to be made in PMMA$(n = 1.449624)$, and all field lenses are assumed to be made of BK7 glass.

A. Tilted Spherical Mirror SDD

The first design to be simulated is the tilted spherical mirror SDD shown in Fig. 3. Fig. 13 shows the simulation results that correspond to the tilted spherical mirror SDD for a shift displacement of 2Δ (i.e., equivalent to 500 μm for $\Delta = 250$ μm). In the bottom part of the figure, we can see the layout for this particular SDD; there are two microlenses, each with a 250-μm

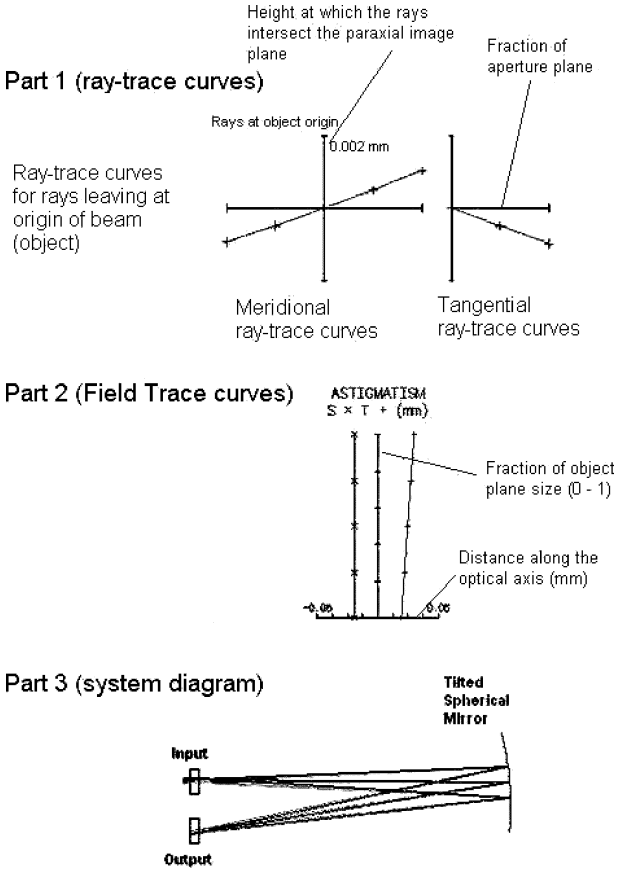

Fig. 13. Ray-trace analysis for a tilted spherical mirror SDD for a 2Δ shift. The figure is divided into three different parts. The ray-trace curves on part 1 shows that the main aberration is astigmatism (each pair of ray-trace curves are straight line where the tangential and meridional trace have different slopes). The field-trace curve of part 2 measures the astigmatism of the system as 0.03927 mm, and part 3 shows a schematic for the tilted spherical mirror SDD.

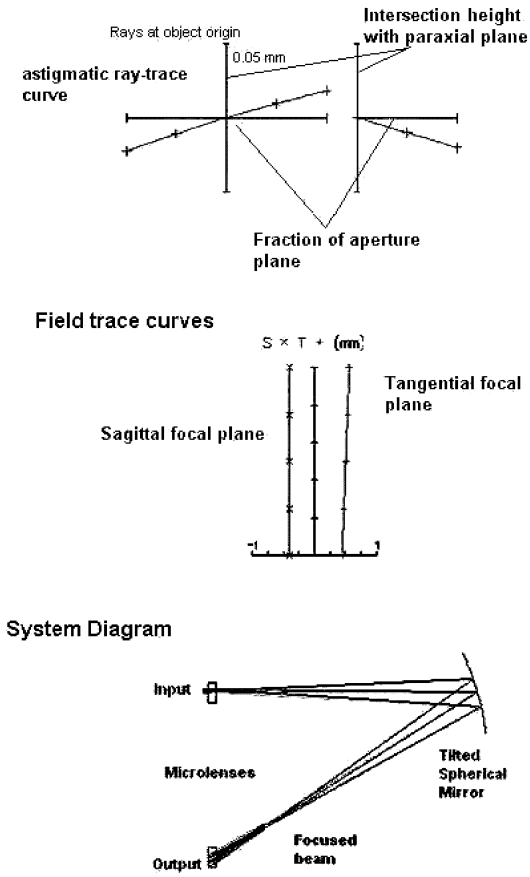

Fig. 14. Ray-trace analysis for a tilted spherical mirror SDD for an 8Δ shift. Part 1 of the system shows that the main aberration is astigmatism; from the change in scale of the ordinate axis, we can see that the astigmatism has increased from the 2Δ case. This is corroborated in part 2 of the figure where astigmatism is measured as 0.84 mm. In part 3, we can see that the rays are focusing before the second microlens field.

diameter. Each microlens is a plano convex lens with 1.627-mm radius of curvature and 0.1-mm thickness. The distance from the microlens to the spherical tilted mirror is 3.1746 mm, and the radius of curvature of the spherical mirror is also 3.1746 mm. To cause this particular shift, the tilt angle of the spherical mirror is calculated by OSLO and set at 4.4311°. From the ray-intercept curves on the top of the figure, we can appreciate that the main aberration present is astigmatism, which is expected because the light goes through the center of the microlenses but is incident on the spherical mirror at an angle. The astigmatism for this particular setup is measured as 0.03927 mm.

We now present the simulations for the same SDD design but for a shift displacement of 8Δ (i.e., equivalent to 2000 μm for a pitch of $\Delta = 250$ μm). The system is shown in Fig. 14; the optical elements and distance between the lenses and the spherical mirror is the same as the one of Fig. 13, and only the tilted angle of the spherical mirror changes. As in the previous case, the main aberration observed is astigmatism. The titled angle of the spherical mirror is set for this shift at 15.997°. The consequence of the increase in the tilted angle is reflected as an increase in astigmatism, which for the present case is measured at 0.840 mm, compared to 0.03927 mm for 2Δ. It can also be seen, from part 3 on the figure, that the beams are not focusing on the second microlens. The reason for this is that, as we rotate the spherical mirror, the image plane, (that is located 3.1746 mm away from the spherical mirror) also rotates describing a circle (with its center at the middle point of the spherical mirror). To correct this curved image plane, it would be necessary to include additional optical element(s). We did not detect this in the design of Section III-A because we were working in the paraxial regime, which is no longer valid for the tilted angle values used in the current simulation.

B. Roof Prism SDD

We now evaluate the roof prism SDD for a shift displacement of 500 μm (2Δ) using OSLO. The roof prism SDD was shown in Fig. 6. We are assuming that the roof prism is made of PMMA with a 15-μm-radius spot size at the image plane of input/output plane. From Section III-B, we calculate the distance between the curved surface of the microlens and the input plane as 0.4402 mm from the same image plane, the thickness of the microlens as 0.263075 mm, and the radius of curvature of the microlens as 0.1979 mm.

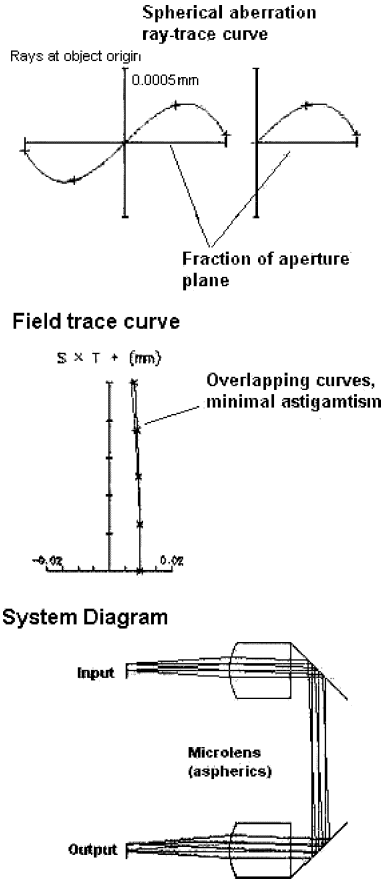

Fig. 15. Ray-lens intercept curves and field-trace curve for roof prism SDD using aspheric lenses. Part 1 of the figure shows that the main aberration; is spherical aberration; the ordinate axis scale of 0.0005 mm indicates to us that this aberration can be ignored. The overlapping of the sagittal and tangential curves in part 2 indicates that the contribution of astigmatism is minimal and can also be ignored. This reduction in aberrations is due to the use of aspheric microlenses in the SDD design.

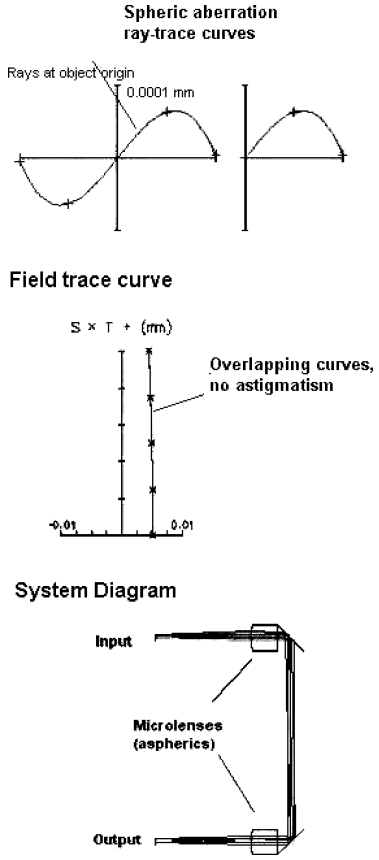

Fig. 16. Ray-lens intercept curves and field-trace curve for an 8Δ roof prism SDD using aspheric lenses. We can see that a displacement of 8Δ has a minimal increase in the contribution of spherical aberration and astigmatism. The aspheric microlenses prove to be very helpful in reducing the presence of aberrations even for increased displacements.

The astigmatism and spherical aberrations can be reduced using an aspheric microlens at the input and output of our roof prism SDD. Fig. 15 shows the ray-intercept curves and field plots for the roof prism SDD using aspheric lenses with a conic constant of -1.22. In the ray-intercept curves, we can see that astigmatism has been almost eliminated and that the main remaining aberration is spherical aberration. It is important, however, to note that the amount of spherical aberration is very small.

We now evaluate the system that causes a shift displacement of 2000 μm (8Δ). The layout of the SDD and the ray-trace analysis curves are shown in Fig. 16. To have the desired shift, it is necessary to change the radius of curvature and distance from the input/ouput plane to the curved surface of the microlens. We use the formulas described in Section III-B to make the appropriate changes. The distance from the plane of input/output plane to the curved surface of the microlens is now set at 0.9575 mm, and the radius of curvature of the microlens is set for this case at 0.4305 mm. As in the previous case, we use aspheric surfaces to reduce the astigmatism and spherical aberration of the system. For this case, the conic constant is set at -1.22. From the ray-trace curves, we can appreciate that the effect of astigmatism is minimal, and that the only aberration present is a minimum amount of spherical aberration.

Even though a significant increase in the shift displacement has been made, the change in the quantity and quality of the exhibited aberrations is minimal in this SDD design. The only drawback is that different optical elements have to be designed for different shift displacements and that the position of each SDD column with respect to the plane of input/output plane has also to be different, which may difficult the alignment.

C. Lens Train SDD

As in the case of the tilted spherical mirror SDD and the roof prism SDD, we simulate a lens train SDD for a 500- and a 2000-μm shift using OSLO. The design of the lens train SDD is shown in Fig. 10(b). We are assuming a 15-μm-radius spot size at the image plane of input/output plane, the curve surface of the micromirror is placed 1.599 mm from the same image plane, and the radius of curvature of each of the spherical mirrors is 3.253032 mm. We are assuming that the lens trains are also made of PMMA.

The ray-intercept curves, the field-plot curves, and a diagram of the lens train SDD for the 500- and 2000-μm shift cases

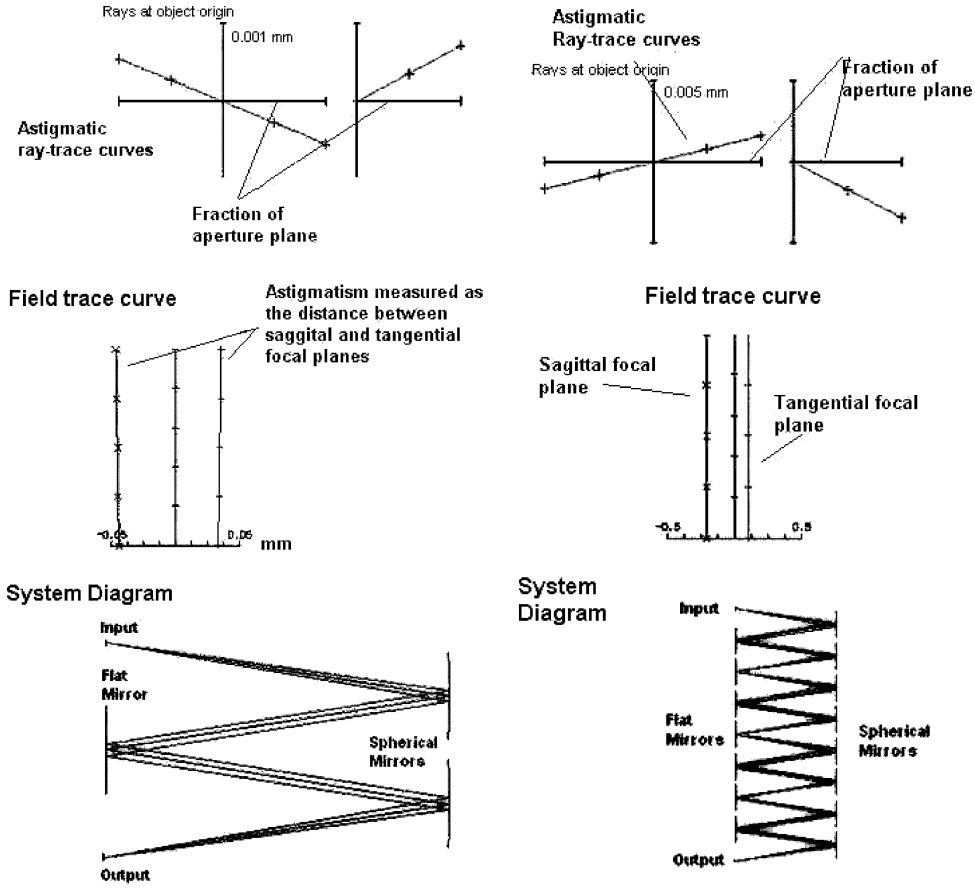

(a) 2Δ (b) 8Δ

Fig. 17. Ray-lens intercept curves and field-trace curve for lens train SDD. (a) 2Δ shift displacement; (b) 8Δ shift displacement. In both cases, we can see, from the ray-intercept curves of part 1, that the main aberration is astigmatism, which when measured, from the field-trace curves of part 2, is 0.07764 mm for 2Δ and 0.3119 mm for 8Δ. This particular SDD design may be modified to produce shifts larger than 64Δ.

are shown in Fig. 17(a) and (b), respectively. The line-shaped ray-intercept curves (left column of Fig. 17) indicate that the main aberration of the system is only astigmatism. In the field-plot curves, we can appreciate that the astigmatism remains constant along the object with an average value of 0.07764 and 0.3119 mm, respectively.

It is, therefore, fair to say that as the shift displacement caused by the lens train SDD increases, so will the aberrations produced by it. The advantage of the lens train over the roof prism SDD is that the lens train does not limit the possible shift displacement produced. This advantage will become relevant when large OXC (>64 outputs) devices have to be designed. For OXC devices with a small number of outputs, it will be sufficient to work with the roof prism SDD.

V. Binary Cell Simulations

One conclusion we obtained from Section IV is that the roof prism SDD has the best performance of the SDD designs analyzed in terms of aberrations. Unfortunately, the roof prism SDD has a limit in the size of displacement it can produce. This limit is set specifically by the microlens diameter. Therefore, the roof prism SDD is the best choice until this limit is reached. Beyond this limit, the lens train SDD is the most obvious choice. Unfortunately, the lens train SDD increases aberrations for larger displacements, and so it will be desirable to improve the lens train design to correct the aberration or at least minimize them.

In the current section, we will present an OSLO simulation for a binary cell that uses roof prism SDD as the shifting device. We design three different roof prism SDD to cause a spot shift of $\Delta, 2\Delta$, and 4Δ. The simulated binary OXC system is a 12-bounce system necessary to allow for eight possible outputs. We will present the bounce pattern and ray analysis curves for the cases when a beam goes to the zeroth output and when it goes to the fifth output. We will also present the accumulated astigmatism for the seven possible outputs. This will help us to evaluate the effects that the SDD has on the beam quality in terms of aberrations.

Before we start our simulation, we show in Table I the values of d_0, d_1, and R for the different roof prism SDD used in the simulations. As in Sections III and IV we will assume that $w_0 = 15\ \mu$m, $\Delta = 250\ \mu$m, and $\lambda = 1.55\ \mu$m, and that the roof prism is made of PMMA. For all cases, we are assuming that the microlenses have a thickness of 0.263075 mm, which is included in d_1.

TABLE I
ROOF PRISM SDD DESIGN PARAMETERS
(ALL MEASUREMENTS IN MILLIMETERS)

Shift	d_0	d_1	R
Δ	0.3539366	0.513075	0.1591384
2Δ	0.4401659	0.638075	0.197909
4Δ	0.6126244	0.888075	0.2754506

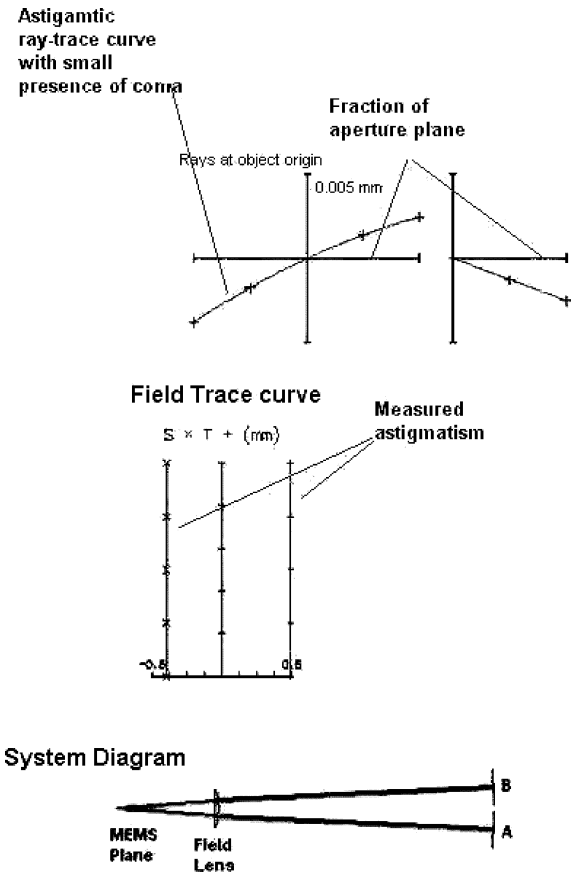

Fig. 18. Ray-trace curves for zeroth output, for the binary White cell OXC. The beams are bouncing exclusively in the null cell. The ray-trace curves of part 1 indicate that the main aberration is astigmatism: the fact that the beams are incident off-axis and at a particular angle on the field lens introduce a slight amount of coma. The presence of coma can be identified by the slight curve that can be seen in the ray-trace curves. From part 2 of the figure, we measure the astigmatism as 0.816735 mm.

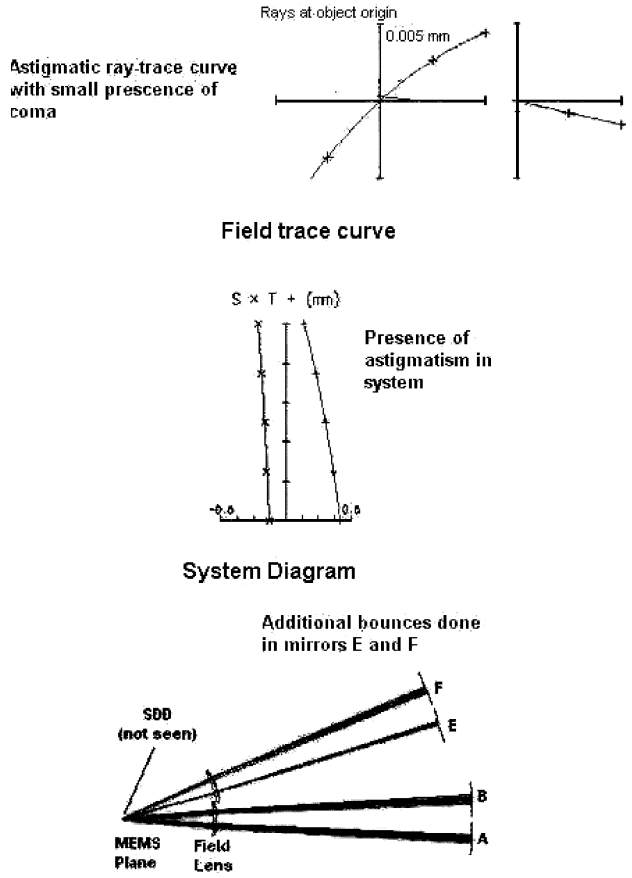

Fig. 19. Ray-trace curves for the fifth output of the binary White cell OXC. From part 1, we can see that the main aberration is still astigmatism, although the presence of coma has increased. In this case, the beams are sent to the SDD two times. This increases the astigmatism to 1.052497 mm.

We refer the reader back to Fig. 1 for the binary White cell OXC to be simulated. We will assume that the null cell is formed by a BK7 meniscus field lens with a 400-mm focal length and two 609.8-mm radius of curvature spherical mirrors. For both lateral wings, we will also assume that we are using 350-mm focal length BK7 meniscus lenses and 609.8-mm radius of curvature spherical mirrors. We are assuming a two-state MEMS with a tilting angle of $\pm 10^{\circ}$.

We start our analysis with Fig. 18, which represents the ray-intercept curves when the beam bounces exclusively in the null cell. We expect this to be the best case of the binary system because there is no shifting of the beam by any SDD element. From the ray-trace curves (part 1), we can see that the main aberration is astigmatism; there is a slight curvature in the graph, however, which represents coma that appears because the beams are incident off-axis on the field lens and at a tilted angle. The average astigmatism is measured at 0.816735 mm.

We now show in Fig. 19 the ray-trace analysis for a 5Δ shift. The process of how the beam is sent to the fifth outputs can be seen in the bounce pattern of the "white" beam in Fig. 2. From the ray-trace curves, we can see that the main aberration is again astigmatism. It is interesting to see that the curves are quite similar to those presented in Fig. 18 for the zeroth output. This is a good indication that the aberrations remain similar even after the introduction of several structures like the SDD.

In Table II, we summarize the amount of astigmatism presented in the system for the eight different possible outputs. There is an important aspect to note in the results shown in the table: Not only the outputs 0, 1, 2, and 4 present a similar total astigmatism, but also the total astigmatism is lower than that for the rest of the outputs (i.e., outputs 3, 5, 6, and 7). The explanation of this is that the outputs 1, 2, and 4 need only one SDD element to shift the beam the required distance, while the outputs 3, 5, 6, and 7 require going through several SDD structures, thus increasing the aberrations.

TABLE II
ACCUMULATED ASTIGMATISM FOR AN EIGHT-OUTPUT BINARY CELL OXC SYSTEM (ALL MEASUREMENTS IN MILLIMETERS)

Output Number	Sagittal Astigmatism	Tangential Astigmatism	Total
0	0.376158	-0.440577	0.816735
1	-0.391409	0.509484	0.900893
2	-0.322928	0.502422	0.82535
3	0.501870	-0.597421	1.099291
4	-0.413074	0.494959	0.908033
5	0.477957	-0.57454	1.052497
6	0.478084	-0.582042	1.060126
7	-0.626611	0.480742	1.107353

A. Aberration Effect in Coupling Losses

Aberrations are important because they can affect the coupling of the beam to an optical fiber. From our simulations we could see that the main aberration presented is astigmatism. The presence of astigmatism has been corroborated in other experiments [24], [33], [34]. To calculate the dependence of astigmatism on coupling, we use the OSLO fiber coupling feature. We assumed the fiber to be a single-mode fiber normally aligned to the focal point at the output plane of the White cell OXC. In general, if the astigmatism is less than the depth of focus, we can neglect it. For this system, the depth of focus is 3.2154 mm, compared to a worst-case astigmatism of 1.107353 mm. The criterion for an acceptable beam is ultimately dependent on the summation of all the optical aberrations being smaller than the depth of focus [24]. The OSLO results showed that the coupling losses are 1.73 ± 0.5 dB for the cases simulated. This result is close to the experimental value found for coupling a beam into a single-mode fiber after a White cell system in [20]. The major contributors, however, to the loss in the White cell OXC will come from nonperfect reflectivity of the MEMS micromirror, fiber alignment at the output plane, and alignments of the SDD device.

B. Scaling Up

There are limiting factors that affect the number of outputs in a binary White cell OXC. The number of bounces that can be performed on the White cell affects the loss due to the reflectivity of the MEMS micromirrors. In a parallel research where a White cell configuration have been used to cause optical true-time delays, we have experimentally measured a maximum loss of 4.4 dB after ten bounces when measured with an 818-IR Newport photodetector [33]. Different White cell configurations may provide a higher number of outputs with fewer bounces.

As the number of output increases, the aberrations introduced by the SDD may become a limiting factor. There may not be a single design that can be used for small displacements (i.e., lower than $32\,\Delta$) as well as for long displacements. For example, by simple extrapolation from the data of Table II, we calculate that the aberrations introduced by the roof prism SDD will become critical after 64 outputs. Therefore, by using a binary configuration with a three-state MEMS and a roof prism SDD, it will be possible to get up to 64 different outputs with only 12 bounces, and we can jump to 128 outputs with a corrected lens trains SDD in 14 bounces.

TABLE III
SUMMARY OF RESULTS FOR ASTIGMATISM IN THE SDDS DESIGN PRESENTED (ALL MEASUREMENTS IN MILLIMETERS)

SDD Design	Astigmatism 2Δ	Astigmatism 8Δ
Tilted Spherical Mirror	0.03927	0.840
Roof Prism	0.0012	0.0013
Lens Train	0.0776	0.3119

VI. SUMMARY AND CONCLUSION

In the present paper, we have evaluated three different designs of an SDD to be used in a 3-D free-space OXC system using digital MEMS. The OXC system is based on the optical White cell in a binary configuration.

The results of the evaluation of these three different SDD designs are summarized in Table III. Here, we can see that the roof prism SDD has the better performance for a 2Δ shift and an 8Δ shift. However, we have to consider that the roof prism SDD is limited by the diameter of its microlens, and so to have longer displacements, it would be necessary to increase the size of the microlens. For small displacements, it will be sufficient to use the roof prism SDD; if longer displacements are needed (i.e., >128), it will be necessary to use the lens train SDD.

We use the roof prism SDD to simulate an 1×8 binary White cell OXC system. We found that the astigmatism of the system depends on the number of times a beam is sent to the SDD. From our simulations, we obtain a coupling loss of 1.73 ± 0.5 dB. The main loss contribution, however, at this scale will be the alignment of the SDD and the output fiber as well as the loss associated with the limited micromirror reflectivity. The roof prism SDD can be scaled up to 64 outputs (in 12 bounces). To produce higher output systems (i.e., 128×128), it will be necessary to include a corrected lens train SDD and increase the number of bounces in the system to 14.

REFERENCES

[1] L. Y. Lin and E. L. Goldstein, "Opportunities and challenges for MEMS in lightwave communications," *IEEE J. Sel. Topics Quantum Elect.*, vol. 8, no. 1, pp. 163–172, Jan.–Feb. 2002.
[2] G. I. Papadimitriou, C. Papazoglou, and A. S. Pomportsis, "Optical switching: Switch fabrics, techniques, and architectures," *J. Lightw. Technol.*, vol. 21, no. 2, pp. 384–405, Feb. 2003.
[3] P. B. Chu and S.-S. Lee, "MEMS: The path to large optical crossconnects," *IEEE Commun. Mag.*, vol. 40, no. 3, pp. 80–87, Mar. 2002.
[4] D. J. Bishop, C. R. Giles, and G. P. Austin, "The Lucent lambdarouter: MEMS technology of the future here today," *IEEE Commun. Mag.*, vol. 40, no. 3, pp. 75–79, Mar. 2002.
[5] T.-W. Yeow, K. L. Eddie Law, and A. Goldenberg, "MEMS optical switches," *IEEE Commun. Mag.*, vol. 39, no. 11, pp. 158–163, Nov. 2001.
[6] N. S. Moon and K. Kikuchi, "N × N multiwavelength optical crossconnect based on tunable fiber bragg gratings," *J. Lightw. Technol.*, vol. 21, no. 3, pp. 703–718, Mar. 2003.
[7] M. P. Earnshaw, J. B. D. Soole, M. Cappuzzo, L. Gomez, E. Laskowski, and A. Paunescu, "8 × 8 optical switch matrix using generalized machzehnder interferometers," *IEEE Photon. Technol. Lett.*, vol. 15, no. 6, pp. 810–812, Jun. 2003.

[8] M. Makihara, "Micromechanical optical switches based on thermocapillarity integrated in waveguide substrate," *J. Lightw. Technol.*, vol. 17, no. 1, pp. 14–18, Jan. 1999.
[9] D. K. Yang, "A simulation study of a liquid crystal optical switch based on total internal reflection," *J. Opt. A, Pure Appl. Opt.*, vol. 5, no. 1, pp. 402–408, Jul. 2003.
[10] P. De Dobbelaere, K. Falta, L. Fan, S. Gloeckner, and S. Patra, "Digital MEMS for optical switching," *IEEE Commun. Mag.*, vol. 40, no. 3, pp. 88–95, Mar. 2002.
[11] L. Y. Lin, E. L. Goldstein, and R. W. Tkach, "Free-space micromachined optical switches with submilisecond switching time of large scale optical cross-connects," *IEEE Photon. Technol. Lett.*, vol. 10, no. 4, pp. 525–527, Apr. 1998.
[12] R. T. Chen, H. Nguyen, and M. C. Wu, "A low voltage micromachined optical switch by stress-induced bending," presented at 12th IEEE Int. Conf. Micro Electro Mechanical Systems, Orlando, Fl, 1999.
[13] P. M. Hagelin, U. Krishnamoorthy, J. P. Heritage, and O. Solgaard, "Scalable optical cross-connect switch using micromachined mirrors," *IEEE Photon. Technol. Lett.*, vol. 12, no. 7, pp. 882–884, Jul. 2000.
[14] X. Zheng, V. Kaman, S. Yuan, Y. Xu, O. Jerphagnon, A. Keating, R. C. Anderson, H. N. Poulsen, B. Liu, J. R. Sechrist, C. Pusarla, R. Helkey, D. J. Blumenthal, and J. E. Bowers, "Three-dimensional MEMS photonic cross-connect switch design and performance," *IEEE J. Sel. Topics Quant. Electron.*, vol. 9, no. 2, pp. 571–578, Mar.–Apr. 2003.
[15] D. T. Neilson, R. Frahm, P. Kolodner, C. A. Bolle, R. Ryf, J. Kim, A. R. Papazian, C. J. Nuzman, A. Gasparyan, N. R. Basavanhally, V. A. Aksyuk, and J. V. Gates, "256 × 256 port optical cross-connect subsystem," *J. Lightw. Technol.*, vol. 22, no. 6, pp. 1499–1509, Jun. 2004.
[16] J. Kim, C. J. Nuzman, B. Kumar, D. F. Lieuwen, J. S. Kraus, A. Weiss, C. P. Lichtenwalner, A. R. Papazian, R. E. Frahm, N. R. Basavanhally, D. A. Ramsey, V. A. Aksyuk, F. Pardo, M. E. Simon, V. Lifton, H. B. Chan, M. Haueis, A. Gasparyan, H. R. Shea, S. Arney, C. A. Bolle, P. R. Kolodner, R. Ryf, D. T. Neilson, and J. V. Gates, "1100 × 1100 port MEMS-based optical crossconnect with 4-dB maximum loss," *IEEE Photon. Technol. Lett.*, vol. 15, no. 11, pp. 1537–1539, Nov. 2003.
[17] J. I. Dadap, P. B. Chu, I. Brener, C. Pu, C. D. Lee, K. Bergman, N. Bonadeo, T. Chau, M. Chou, R. Doran, R. Gibson, R. Harel, J. J. Johnson, S. S. Lee, S. Park, D. R. Peale, R. Rodriguez, D. Tong, M. Tsai, C. Wu, W. Zhong, E. L. Goldstein, L. Y. Lin, and J. A. Walker, "Modular MEMS-based optical cross-connect with large port-count," *IEEE Photon. Technol. Lett.*, vol. 15, no. 12, pp. 1773–1775, Dec. 2003.
[18] O. Jerphagnon, R. Anderson, A. Chojnacki, R. Helkey, W. Fant, V. Kaman, A. Keating, B. Liu, C. Pusaria, J. R. Sechrist, D. Xu, S. Yuan, and X. Zheng, "Performance and applications of a large port-count and low-loss photonic cross-connect systems for optical networks," in *15th Annu. Meeting IEEE LEOS*, 2002, vol. 1, pp. 299–300.
[19] H. Laor, "MEMS mirrors applications in optical cross-connects," presented at the IEEE LEOS Summer Topical Meetings: Optical MEMS, Monterey, CA, 1998.
[20] B. L. Anderson, V. Argueta-Diaz, F. Abou Galala, G. Radhakrishnan, and R. J. Higgins, "Optical cross connect switch based on tip/tilt micromirrors in a White cell," *IEEE J. Sel. Topics Quantum. Electron.*, vol. 9, no. 2, pp. 579–593, Mar.–Apr. 2003.
[21] V. Argueta Diaz and B. L. Anderson, "Reconfigurable photonic switch based on a binary system using the White cell and micromirror arrays," *IEEE J. Sel. Topics Quantum. Electron.*, vol. 9, no. 2, pp. 594–602, Mar.–Apr. 2003.
[22] J. U. White, "Long optical paths of large aperture," *J. Opt. Soc. Amer.*, vol. 32, pp. 285–288, 1942.
[23] J. U. White, "Very long optical paths in air," *J. Opt. Soc. Amer.*, vol. 66, pp. 411–416, 1976.
[24] R. L. Higgins, N. K. Nahar, and B. L. Anderson, "Design and demonstration of a switching engine for a binary true-time-delay device that uses a White cell," *Appl. Opt.*, vol. 42, no. 23, pp. 4747–4757, Aug. 2003.
[25] I.-K. Cho, K. B. Yoon, S. H. Ahn, M. Y. Jeong, H.-K. Sung, B. H. Lee, Y. U. Heo, and H.-H. Park, "Board-to-board optical interconnection system using optical slots," *IEEE Photon. Technol. Lett.*, vol. 16, no. 7, pp. 1754–1756, Jul. 2004.
[26] S. Voigt, S. Kufner, A. Kufner, and I. Frese, "A refractive free-space microoptical 4 × 4 interconnect on chip level with optical fan-out fabricated by the liga technique," *IEEE Photon. Technol. Lett.*, vol. 14, no. 10, pp. 1484–1486, Oct. 2002.
[27] M. Kagami, A. Kawasaki, and H. Ito, "A polymer optical waveguide with out-of-plane branching mirrors for surface-normal optical interconnections," *J. Lightw. Technol.*, vol. 19, no. 12, pp. 1949–1955, Dec. 2001.
[28] B. E. A. Saleh and M. C. Teich, *Fundamentals of Photonics*. New York: Wiley, 1991.
[29] C. Pollock, *Fundamentals of Optoelectronics*. Homewood, IL: Irwin, 1995, ch. 10.
[30] W. J. Smith, *Modern Optical Engineering*, 2nd ed. New York: McGraw-Hill, 1990.
[31] R. E. Fischer and B. Tadic-Galeb, *Optical System Design*. New York: McGraw-Hill, 2000.
[32] *OSLO: Optics Reference,* Lambda Research Corporation, Littleton, MA, 2001.
[33] C. M. Warnky, R. Mital, V. Argueta-Daz, and B. L. Anderson, "Demonstration of a quartic cell, a free-space true-time delay device based on the White cell," *J. Lightw. Technol.*, to be published.
[34] V. Argueta-Daz and B. L. Anderson, "Optical cross-connect system based on the white cell and 3-state mems: Experimental demonstration of the quartic cell," *Appl. Opt.*, to be published.

Victor Argueta-Diaz (S'03–M'04) received the B.S. degree in telecommunication engineering from the National Autonomous University of Mexico, Mexico City, Mexico, in 1999, and the M.S. and Ph.D. degrees in electrical engineering from The Ohio State University, Columbus, in 2002 and 2005, respectively.

He spent two years in industry, working on optochemical sensors and wireless communication. He is currently a Postdoctoral Researcher at the Center of Applied Science and Technology, Mexico City. His current research interests include devices for optical communication systems, optical sensors, and MEMS.

Dr. Argueta-Diaz is a member of the Optical Society of America.

Betty Lise Anderson (S'75–M'78–SM'95) received the B.S. degree in electrical engineering from Syracuse University, Syracuse, NY, in 1978, and the M.S. and Ph.D. degrees in materials science and electrical engineering from the University of Vermont, Burlington, in 1988 and 1990, respectively.

She spent nine years in industry at, among other companies, Tektronix, Inc., GTE Laboratories, and Draper Laboratories. She is currently a Professor at The Ohio State University, Columbus, in the Department of Electrical and Computer Engineering. She is the coauthor (with Richard L. Anderson) of *Fundamentals of Semiconductor Devices* (McGraw-Hill, 2005). Her current research interests include analog optical signal processing, devices for optical communication systems, coherence, and semiconductor devices.

Prof. Anderson is a member of the Optical Society of America. She is an Associate Editor for the IEEE JOURNAL OF QUANTUM ELECTRONICS.